Predictive Finite-State Control—When to Use and When Not

Joachim Holtz, *Life Fellow, IEEE*

***Abstract*—A multistep predictive algorithm eliminates overshoots of the current vector outside the boundary circle while the processor identifies the next optimal switching state vector following a boundary transition. The predictions of the current vector trajectories refer to a simplified machine model consisting only of the leakage inductance. Nevertheless is good accuracy of the predictions achieved. Operation at low switching frequency minimizes both harmonic distortion and switching losses. Using higher switching frequencies does not lead to noticeable improvement over ordinary carrier modulation. Maximum fundamental output voltage is achieved by predictive overmodulation.**

***Index Terms*—Medium-voltage drives, optimum pulsewidth modulation, overmodulation, predictive control.**

I. INTRODUCTION

THE control of the power flow between two electrical systems is generally done using pulsewidth modulated converters. Recent advancements of the technology are characterized by increased power ratings on one hand, and the advent of new modulation techniques on the other hand.

The potentiality of predictive control was first published in 1983 [1], [2], but has remained unnoticed by the scientific community for many years. Only recently have a great many publications appeared on that method [3]–[9]. Biannual conferences were held [10], [11]. Papers of a special section on predictive control cover three volumes of IEEE TRANSACTIONS ON INDUSTRIAL ELECTRONICS [12]–[14]. Also, two books on predictive control have appeared [16]–[18]. An overview of pulsewidth modulation and predictive control is given in [7].

It is a common misconception of the capability of predictive control that operation at higher switching frequency reduces the harmonic content of the ac currents. The opposite is true: the modulation quality tends to get worse than the computationally most simple method of space vector modulation.

An adequate strategy for predictive control will be demonstrated by describing the performance of this method under the following conditions.

1) The model consists only of the leakage inductance of the machine.
2) The boundary dimensions are large to enable operation at switching frequencies of a few 100 Hz.
3) Multistep prediction is employed to eliminate current overshoot.
4) Receding horizons are not considered.

The advent of power semiconductor devices having maximum ratings of 6.5 kV and 8 kA requires their application at extreme low switching frequencies. Only optimum modulation methods are capable of maintaining the switching losses at a tolerable level. Replacing pulsewidth modulation techniques by predictive algorithms is the answer.

The objective of a predictive algorithm is to select the most suited switching state from the set of discrete switching states of a particular power converter. Such predictive controller commands a finite control set.

Although predictive algorithms are preferred for controlling high-power multilevel inverters, a two-level inverter topology will be used in the analysis for better insight. The conclusions are nevertheless valid: the optimal switching state is always one of those three vectors located in a close neighborhood to the vector of the induced machine voltage, independently of the number of voltage levels.

This article is organized as follows. The predictive algorithm, its extension to multistep prediction, and the large-signal response to higher transients are explained in Section II. Section III describes predictive overmodulation, and Section IV demonstrates that the influence of varying machine parameters is ineligible. Section V proves that predictive control is an optimal modulation method.

It is the objective of this article to demonstrate that predictive control

1) produces optimal results only at low switching frequency operation, as shown in Section V;
2) does not require high-frequency state variable updates;
3) does not require elaborate models for predictions.

II. PREDICTIVE ALGORITHM

A. Principle of Operation

A simplified machine model in Fig. 1 is composed of switching state vector $\boldsymbol{u}_\mathrm{k}$ as the input voltage vector, and the estimated total leakage inductance $\hat{l}_\sigma$

$$i_\mathbf{s} = \frac{u_\mathbf{k} - \hat{u}_\mathbf{i}}{\hat{l}_\sigma} \tag{1}$$

Manuscript received November 25, 2020; revised February 20, 2021, June 5, 2021, and August 31, 2021; accepted October 14, 2021. Date of publication October 20, 2021; date of current version December 31, 2021. Recommended for publication by Associate Editor R. Kennel. *(Corresponding author: Joachim Holtz.)*

The author is with the Electrical Machines and Drives, University of Wuppertal, 42097 Wuppertal, Germany (e-mail: j.holtz@ieee.org).

Color versions of one or more figures in this article are available at https://doi.org/10.1109/TPEL.2021.3121277.

Digital Object Identifier 10.1109/TPEL.2021.3121277

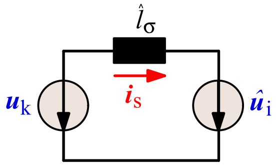

Fig. 1. Model approximation.

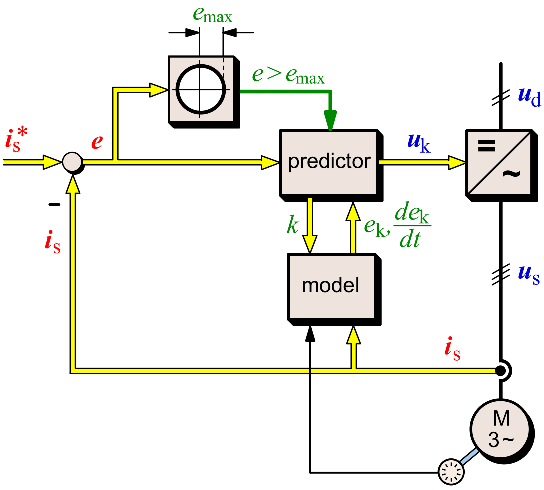

Fig. 2. Predictive controller signal flow graph.

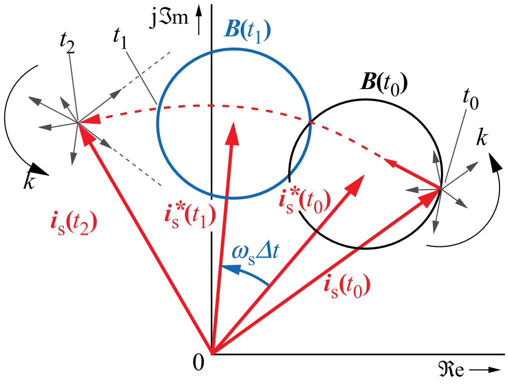

Fig. 3. Space vectors and boundary circles.

while the estimated vector of the back EMF $\hat{\boldsymbol{u}}_i$ is provided by a superimposed vector control system (see Fig. 2).

Predictive control is an event-triggered closed-loop pulsewidth modulation scheme, controlled by the stator current reference vector $\boldsymbol{i}^*$ with the stator current vector $\boldsymbol{i}$s as the feedback signal. The signal flow graph is shown in Fig. 2. The predictor is activated whenever the magnitude $e = |i_s{}^* - i_s|$ of the current error exceeds a given maximum value $e_{\max}$. This happens at time t_0.

The current error $\boldsymbol{e}$ is continuously monitored. The predictor sends all possible switching states k to the model whenever the condition $\boldsymbol{e} > |e$ max$|$ holds. The model then returns the respective values of the current signal $\boldsymbol{i}_s(k)$ and its derivative d$\boldsymbol{i}_s$(k)/dt. These serve to predict k error trajectories, approximated by straight lines as shown in Fig. 3.

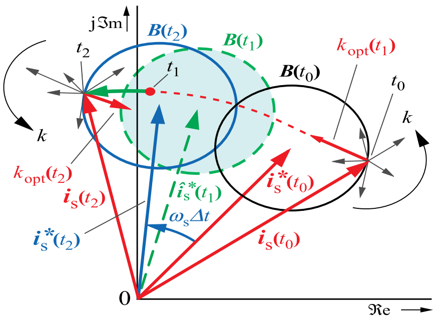

Fig. 4. Multistep prediction.

The objective function determines the optimal switching state vector k^{opt}

$$\frac{\Delta t\,(k)}{n_c} \rightarrow \max \tag{2}$$

where

$$\Delta t\,(k) = \frac{\boldsymbol{i}_{\mathbf{s}}\,(t_1) - \boldsymbol{i}_{\mathbf{s}}\,(t_0)}{d\boldsymbol{i}_{\mathbf{s}}/dt} \tag{3}$$

is the time during which the current vector remains within the boundary circle, and n_c is the number of commutations required to apply the optimal vector.

The boundary circle $\boldsymbol{B}$ sets a limit beyond which the stator current vector must not go. The location of its center point is defined by the reference vector $\boldsymbol{i}_s{}^*$.

As time elapses, the reference vector displaces from $\boldsymbol{i}_s{}^*(t_0)$ to $\boldsymbol{i}_s{}^*(t_1)$, and the boundary area displaces from $\boldsymbol{B}(t_0)$ to $\boldsymbol{B}(t_1)$, both at the angular stator velocity ω_s. At $t1$, there occurs a boundary intersection, which starts the prediction of the future current trajectories. The evaluation of (2) and (3) for all switching states k and the selection of the optimum switching state introduces a time delay. The result is available at t_2. By this time has the current vector gone far beyond the boundary circle which creates a substantial current overshoot. Additional commutations are needed to make the current return into the boundary.

The graph shows that the resulting current trajectories may not allow the current vector returning into the boundary circle with only one commutation. Periodic overshoots result in even more harmonic current distortion, which is a common deficiency of event-triggered modulation techniques: the occurrence of a trigger event does not immediately produce the required action. A delay time elapses until the next action is computed. This drawback is cured in the following.

B. *Multistep Prediction*

The method is used to avoid current overshoots. It is explained with reference to Fig. 4. It predicts the following:

1) the trajectory of the reference vector $\boldsymbol{i}_s{}^*$, the trajectory of the current vector $\boldsymbol{i}_s$, and the time instant t_2 of its boundary transition,
2) the current vector is(t_2) and the induced voltage $\hat{\boldsymbol{u}}_i(t_2)$, both to update the model;
3) the k possible current trajectories, and from these
4) the optimal switching state vector $\boldsymbol{u}_k$ opt(t_2);

5) the squared error vector $\boldsymbol{e}^2$, advanced in time by $\Delta t_e = t_1 - t_0$, where Δt_e is the time required for predicting positions 1) – 3).

The above predictions rely on linearized error trajectories $\boldsymbol{e}(t,k) = \boldsymbol{i}_s{}^*(t,k) - \boldsymbol{i}_s(t,k)$, and is expressed as

$$\boldsymbol{e}(t,k) = \boldsymbol{e}(t_0) + \left.\frac{d\boldsymbol{e}(t,k)}{dt}\right|_{t_0} \cdot \Delta t \tag{4}$$

where $\Delta_t = t_2 - t_0$. We have from (4) that

$$\left.\frac{d\boldsymbol{e}(t,k)}{dt}\right|_{t_0} = \left.\frac{d\boldsymbol{i}_{\mathbf{s}}^*(t)}{dt}\right|_{t_0} - \left.\frac{d\boldsymbol{i}_{\mathbf{s}}(t,k)}{dt}\right|_{t_0}. \tag{5}$$

The two derivative terms in (5) are

$$\left.\frac{d\boldsymbol{i}_{\mathbf{s}}(t,k)}{dt}\right|_{t_0} = \frac{\boldsymbol{u}_{\mathbf{k}}(t_0,k) - \boldsymbol{u}_{\mathbf{i}}(t)|_{t_0}}{\hat{l}_\sigma} \tag{6}$$

and as a linear extrapolation

$$\left.\frac{d\hat{\boldsymbol{i}}_s^*(t)}{dt}\right|_{t_0} = \frac{\boldsymbol{i}_s^*(n) - \boldsymbol{i}_s^*(n-1)}{t_n - t_{\mathbf{n-1}}} \tag{7}$$

where n and $n - 1$ mark the last two samples of the reference vector.

Identifying the optimal switching state using the multistep prediction method exploits the fact that the magnitudes of the error vector at 20 and at the next boundary intersection to zero are identical. The calculations start with squaring the error function: open 4, which yields

$$\begin{aligned} e^2(t,k) &= e^2(t,k) \circ e^{2*}(t,k) \\ &= e^2(t_0) + 2e(t_0)\frac{de(t,k)}{dt}\Delta t + \left(\frac{de(t,k)}{dt}\Delta t\right)^2 \end{aligned} \tag{8}$$

where

$$\frac{de(t,k)}{dt} = \sqrt{\left.\frac{de(t,k)}{dt}\right|_{t_0} \circ \left.\frac{de^*(t,k)}{dt}\right|_{t_0}} \tag{8a}$$

since the square $\boldsymbol{x}^2$ of a complex variable $\boldsymbol{x}$ is the inner product $\boldsymbol{x}^\circ\, \boldsymbol{x}^*$. Variable $\boldsymbol{x}^*$ is the conjugate complex of $\boldsymbol{x}$.

The squared functions appear in Fig. 5 as parabolic curves. The dotted green line represents the squared error at $t < 0$, i.e., before the prediction has been started.

The objective function (2) commands maximizing the time interval from $t = t_0$ until the next intersection. The number n_c of commutations in (2) is a penalty. Switching state $k = 3$ in Fig. 5 is only optimal if it can be applied by a single computation, otherwise $k = 1$ may be a better choice.

Equation (8) is written as

$$e^2(t,k) = e^2(t_0) + a_1\Delta t + a_2\Delta t^2. \tag{9a}$$

Adding the term $\boldsymbol{e}^2(t,k)$ at the right of (9a) yields

$$e^2(t,k) = e^2(t_0) + a_1\Delta t + a_2\Delta t^2 = e^2(t,k) \tag{9b}$$

from which we obtain the modified objective function

$$\Delta t = -\frac{a_1}{a_2}\frac{1}{n_c} \rightarrow \max \tag{9c}$$

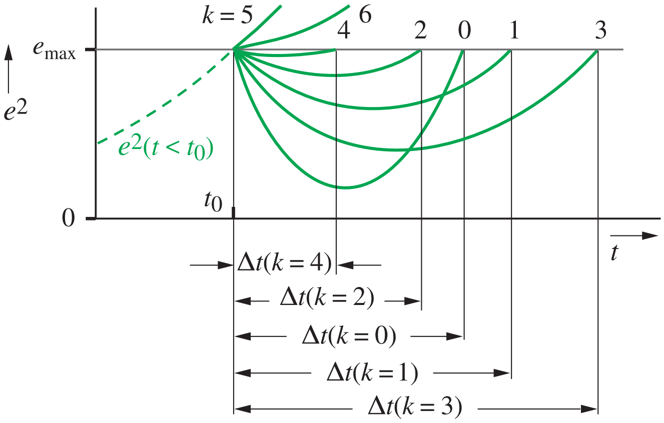

Fig. 5. Squared error functions.

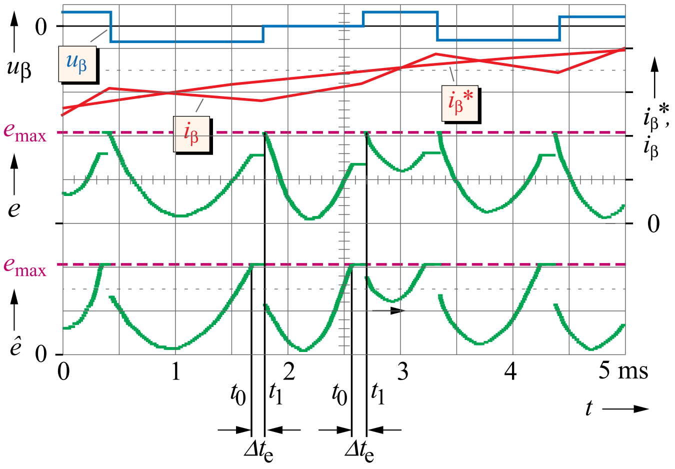

Fig. 6. System variables at multistep prediction.

in which $e^2(t_0)$ is eliminated and

$$a_1 = 2e(t_0)\left.\frac{de(t,k)}{dt}\right|_{t_0}, \quad a_2 = \left(\left.\frac{de(t,k)}{dt}\right|_{t_0}\right)^2. \tag{9d}$$

The solution of (9) for all k provides the optimal switching state $k_{\text{opt}}(t_2)$. The processing of data (9) is completed at $t = t_1$ as shown in Fig. 4. The remaining time difference $t_2 - t_1$ is a safety margin, marked as a green line. Switching state $k\text{opt}(t_2)$ is activated at the next boundary transition.

As the full computing capability of the processor is needed for the optimization, the output of the squared error signal e^2 and its predicted value $\hat{e}^2$ is discontinued during the respective time intervals Δt_0. Only their last values that remain in the respective memory cells are seen in Fig. 6. The waveforms are displayed over a portion of the fundamental interval in this graph.

With the optimum switching states being applied, the current vector continues moving toward another boundary condition. The next cycle to calculate an optimal switching state is started at instant t_0, the same way as illustrated in Fig. 4. The boundary intersection occurs when the current vector has caught up with the moving boundary circle at $t = t_2$. The optimum switching states vector is activated without delay.

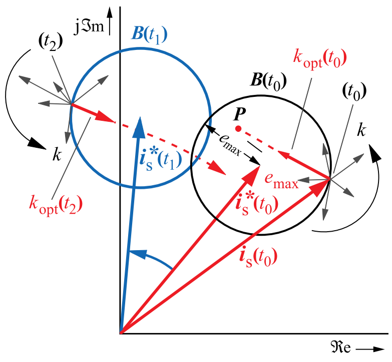

Fig. 7. Trajectories at large-signal error.

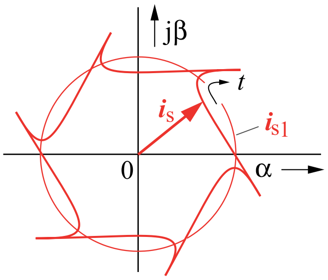

Fig. 8. Current trajectory at six-step operation.

C. Large-Signal Error

A large-signal error situation is displayed in Fig. 7. A commanded reference change displaces the reference vector from $\boldsymbol{i}_s^*(t_0)$ to $\boldsymbol{i}_s^*(t_1)$. It increases the error magnitude beyond the radius $|e_{\max}|$ of the boundary circle. The condition

$$|\boldsymbol{i}_\mathbf{s}^* - \boldsymbol{i}_\mathbf{s}| >> e_{\max} \tag{10}$$

then holds, indicating that the current vector locates outside the boundary circle $\boldsymbol{B}(t_0)$. A switching state $k_{\text{opt}}(t_2)$ is computed, evaluating the inner vector product

$$\left(\boldsymbol{i}_\mathbf{s}^*(n) - \boldsymbol{i}_\mathbf{s}^*(n-1)\right) \circ \boldsymbol{u}_\mathbf{k}^* \to \max \tag{11}$$

for all k, where $\boldsymbol{i}_s^*(n-1)$ is the reference vector that existed before the commanded change. The new switching state is readily available when the current trajectory has come up to point $\boldsymbol{P}$. It forces the current vector back into the interior of the boundary circle.

III. OVERMODULATION

A. Principle of Operation

The maximum fundamental output voltage is obtained in the six-step mode [19], [20]. A two-level inverter activates a sequence in time of the six active switching state vectors during the fundamental period. The resulting current trajectory at six-step operation is shown in Fig. 8 in stationary coordinates, and in Fig. 9(c) in synchronous coordinates. The boundary area has a rectangular shape to fully accommodate the current trajectory.

The modulation range is extended by predictive overmodulation. The circular boundary area is replaced by a larger boundary area of rectangular shape, aligned with the rotor flux vector. Current state variables $\boldsymbol{i}_s$ and $\boldsymbol{i}_s^*$ are referred to in field coordinates.

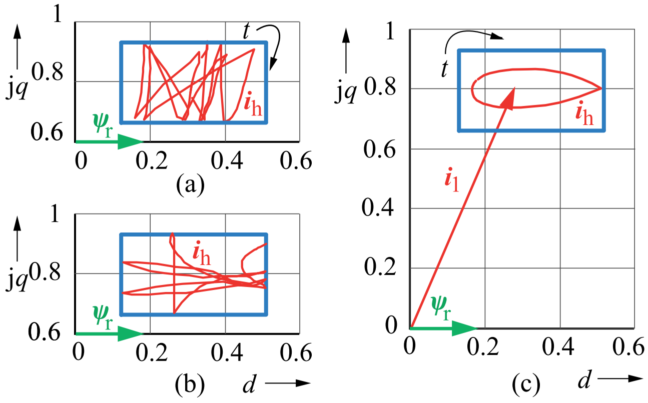

Fig. 9. Rectangular boundary area. (a) Operation at very low speed and $m = 0.2$. (b) Transition to the six-step mode and $m = 0.91$. (c) Six-step mode and $m = 1$.

The modulation index is normalized by the fundamental voltage u_1 at six-step operation

$$m = \frac{u_1}{u_{1\,\mathbf{six-step}}}. \tag{12}$$

While the modulation index is low, e.g., $m = 0.2$ in Fig. 9(a), the current vector hits preferably the horizontal boundaries, thus controlling the q-component of the current vector and setting the machine torque to its commanded value. Medium modulation index occur preferably transitions at the vertical boundaries since errors of the magnetizing d-component occur rarely at the corresponding angular velocity ω_s of the reference frame.

When coming up to the upper limit $m_{\max} = 0.91$ of linear space vector modulation, the transition to higher modulation indices starts the overmodulation mode. The corresponding current trajectory is shown in Fig. 9(a).

As the modulation index further increases, the trajectory of the fundamental current $\boldsymbol{i}_{s1}$ is perpetually reflected at the right boundary [see Fig. 9(b)]. The reflections occur ever more frequently as the modulation index increases. Since the algorithm operates in field coordinates, each reflection at the right boundary forces the current vector to rotate in a positive direction. Operation at the fundamental frequency is thus established.

As the modulation index continues increasing, the number of reflections at the horizontal boundaries tend to reduce, until only those at the right boundary remain. The increasing modulation index lets the reflections at the right boundary increase in number. This leads to a smooth transition to the six-step mode [see Fig. 9(c)]. Only reflections at the right boundary remain when the modulation index has come up to $m = 1$.

B. Numerical Analysis

The stator winding of an induction motor is described by

$$l_\sigma \frac{d\boldsymbol{i}_\mathbf{s}}{dt} = -\left(r_\sigma + j\omega_\mathrm{s} l_\sigma\right)\boldsymbol{i}_\mathbf{s} - \boldsymbol{u}_\mathbf{i} + \boldsymbol{u}_\mathbf{s} \tag{13}$$

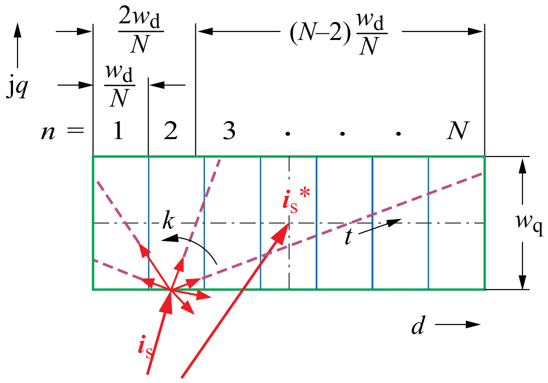

Fig. 10. Rectangular boundary partitioned in N regions. w_d and w_q describe the respective extensions of the rectangle.

where l_σ is the total leakage inductance, r_s describes the effect of the winding resistances of the stator and the rotor, ω_s is the stator frequency, and $\boldsymbol{u}_i$ and $\boldsymbol{u}_s$ are the induced voltage and the stator voltage space vectors, respectively.

The resistive components are neglected. The current trajectories $d\boldsymbol{i}_d/dt$ and $d\boldsymbol{i}_q/dt$ are

$$l_\sigma \frac{di_\mathbf{d}}{dt} = u_\mathbf{d} - r_\sigma i_\mathbf{d} + \omega_\mathbf{s} l_\sigma i_\mathbf{q} \tag{14a}$$

$$l_\sigma \frac{di_\mathbf{q}}{dt} = u_\mathbf{q} - r_\sigma i_\mathbf{q} - \omega_\mathbf{s} l_\sigma i_\mathbf{d} - u_\mathbf{i}. \tag{14b}$$

The high computational load solving these equations is reduced by replacing divisions with multiplications [19]. Equations (14) are inverted and linearized

$$\frac{l_\sigma}{\Delta t_\mathbf{d}} = (u_\mathbf{d} + \omega_\mathbf{s} l_\sigma i_\mathbf{q}) \cdot \frac{1}{\Delta i_\mathbf{d}} \tag{15a}$$

$$\frac{l_\sigma}{\Delta t_\mathbf{q}} = (u_\mathbf{q} - u_\mathbf{i} - \omega_\mathbf{s} l_\sigma i_\mathbf{d}) \cdot \frac{1}{\Delta i_\mathbf{q}} \tag{15b}$$

where Δi_d and Δi_q are the respective spatial distances to the next boundary and Δt_d and Δt_q are the time durations to arrive there. The rectangle error boundary is divided into N regions as shown in Fig. 10. The location at which a q-axis boundary intersection occurs identifies a particular portion of the rectangle, which is $n = 4$ in Fig. 10.

The last term on the right-hand side of (15b) is $1/\Delta i_q \sim 1/w_q = \text{const}$. The last term in (15a) is obtained from a table addressed by n as a pointer. The table variables are

$$\frac{1}{\Delta i_\mathbf{d}} = \frac{N}{n \cdot w_\mathbf{d}}. \tag{16}$$

They are stored in a memory. $N = 16$ regions were programmed when the waveforms in Fig. 9 were recorded.

There are three different boundaries at which the predictive current trajectories can arrive, shown by the dotted trajectory extensions in Fig. 10. The optimal switching state is determined by evaluating the sign of the error, sign($\boldsymbol{i}_s{}^* - \boldsymbol{i}_s$), and the type of error: q-error or d-error. If the current trajectory hits the upper boundary, for example, the q-error is negative and the choice of the optimal switching state is limited to those states that have a negative current gradient. If it hits the lower boundary, the q-error is positive and only states having a positive gradient are selected.

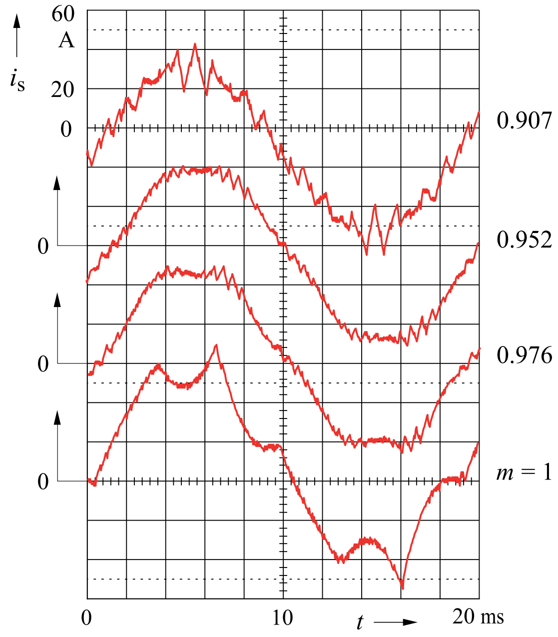

Fig. 11. Smooth transition to predictive overmodulation.

Neglecting the component in quadrature to the respective current trajectory approximates the predicted time duration to reach the next boundary as

$$\Delta t_\mathbf{d}\,(n, k) = \frac{n}{N} w_\mathbf{d} \frac{\hat{l}_\sigma}{u_\mathbf{d} + \omega_\mathbf{s} l_\sigma i_\mathbf{q}} \Delta i_\mathbf{d} \tag{17a}$$

for the horizontal trajectories and

$$\Delta t_\mathbf{q}\,(n, k) = \frac{n}{N} w_\mathbf{q} \frac{\hat{l}_\sigma}{u_\mathbf{q} - \omega_\mathbf{s} l_\sigma i_\mathbf{d}} \Delta i_\mathbf{q} \tag{17b}$$

for the vertical trajectories, where w_d and w_q are the widths of the rectangular boundary.

The objective function for minimum switching frequency is

$$\Delta t_\mathbf{d}\,(n, k) + \Delta t_\mathbf{q}\,(n, k) \rightarrow \max. \tag{18}$$

It is particularly those current trajectories that propagate in d-directions that contribute to reducing the switching frequency.

The oscillogram (see Fig. 11) shows a smooth transition to predictive overmodulation.

IV. PARAMETER SENSITIVITY

The machine model can be of the most simple type. An estimated value of the total leakage inductance l_σ is the only parameter. The resistive components and the magnetizing current are neglected. The extrapolated reference vector (7) may be inaccurate. Satisfactory predictions are nevertheless achieved because only a few discrete output vectors exist from which to choose. There is a high likelihood that the optimum vector is chosen. If a nonoptimal vector is wrongly selected, the next commutation occurs earlier than optimal, which is a minor problem. The superimposed speed controller (see Fig. 12) compensates

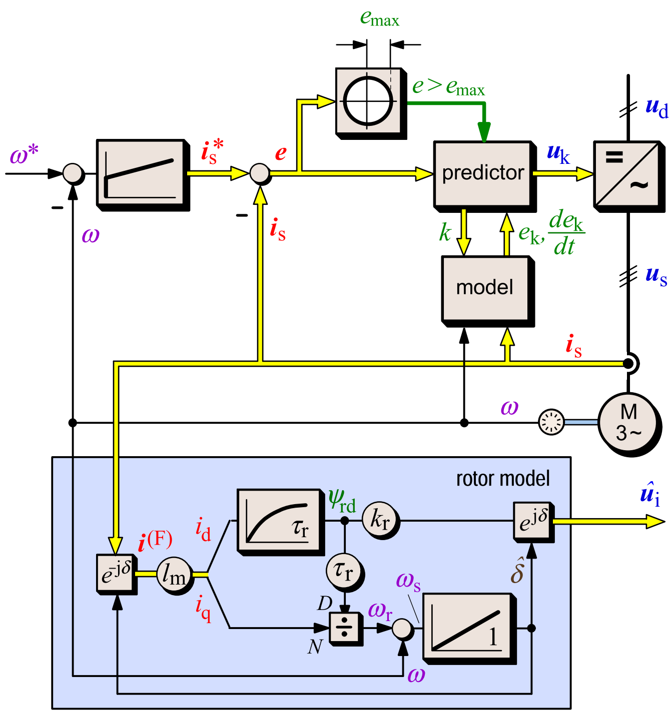

Fig. 12. Superimposed control system.

for whatever deviation has occurred. It uses the rotor model in rotor coordinates

$$\tau_\mathbf{r}\frac{d\boldsymbol{\psi}_\mathbf{r}^{(\mathbf{R})}}{dt}+\boldsymbol{\psi}_\mathbf{r}^{(\mathbf{R})}=-\mathbf{j}\omega_\mathbf{r}\tau_\mathbf{r}\boldsymbol{\psi}_\mathbf{r}^{(\mathbf{R})}+l_\mathbf{m}\boldsymbol{i}_\mathbf{s}^{(\mathbf{R})} \quad (19)$$

where τ_r is the rotor time constant, ω_r is the rotor frequency, $\boldsymbol{\psi}_r$ is the rotor flux leakage vector, and l_m is the mutual inductance. Superscript (R) refers to rotor coordinates.

The condition

$$\omega_\mathbf{r}=\frac{l_\mathbf{m}i_\mathbf{q}}{\tau_\mathbf{r}\psi_\mathbf{d}} \quad (20)$$

is introduced to transform (19) to field coordinates

$$\tau_\mathbf{r}\frac{d\psi_\mathbf{d}^{(\mathbf{F})}}{dt}+\psi_\mathbf{d}^{(\mathbf{F})}=j\omega_\mathbf{s}\tau_\mathbf{r}\psi_\mathbf{r}^{(\mathbf{F})}+l_\mathbf{m}\boldsymbol{i}_\mathbf{s}^{(\mathbf{F})} \quad (21)$$

where

$$\tau_\mathbf{r}\frac{d\hat\psi_\mathbf{rd}}{dt}+\hat\psi_\mathbf{rd}=l_\mathbf{m}i_\mathbf{d} \quad (22)$$

expresses the real component and

$$\hat\delta=\int\left(\frac{l_\mathbf{m}i_\mathbf{q}}{\tau_\mathbf{r}\hat\psi_\mathbf{rd}}+\omega\right)dt \quad (23)$$

is the imaginary component. Variable ω in (23) is the mechanical speed. Equations (22) and (23) are visualized in the lower portion of Fig. 12, which outputs the induced voltage

$$\hat{\boldsymbol{u}}_\mathbf{i}=k_\mathbf{r}\psi_\mathbf{rd}\cdot\exp\left(j\hat\delta\right) \quad (24)$$

where the coefficient k_r is the coupling factor of the rotor, and $\hat\delta$ is the estimated field angle.

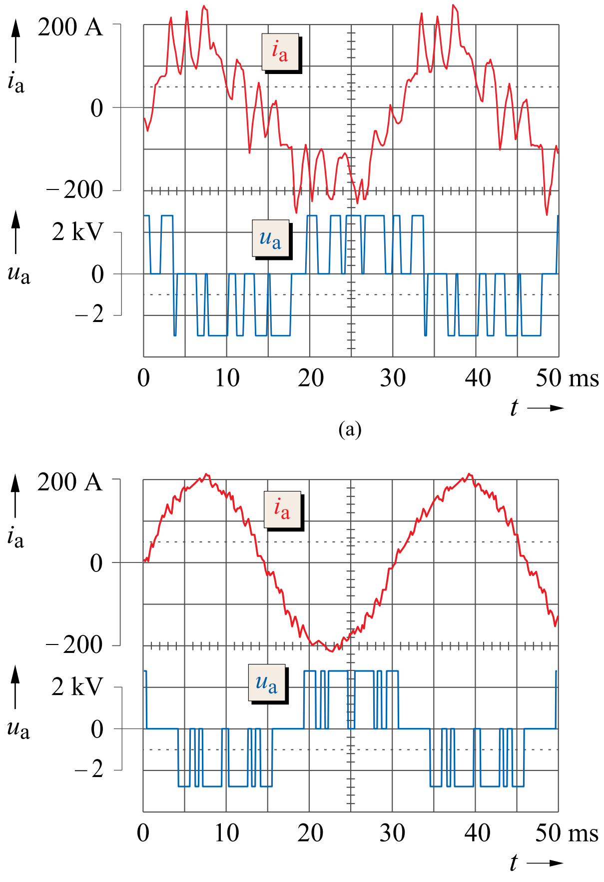

(a)

(b)

Fig. 13. Measured three-level waveforms of the stator current i_a and inverter output potential u_a with switching frequency 200 Hz, fundamental frequency 33 Hz, and modulation index $m = 0.85$. (a) Space vector modulation. (b) Synchronous optimal modulation.

V. IS PREDICTIVE CONTROL AN OPTIMAL METHOD?

To answer this question, the modulation strategy described in this article is compared with other modulation methods. Equidistant pulses are seen at space vector modulation (see Fig. 13(a) [20]), as opposed to variable pulse spacing at synchronous optimal modulation (see Fig. 13(b) [20]). The result is a drastic reduction of current distortion. It is not only the amplitudes of the harmonic current that are high at space vector modulation, but also the phase angle deviations (see Fig. 14).

Only at low switching frequency, an optimal pulse spacing is achieved. Fig. 15 shows the trajectory of the current vector recorded over a full fundamental cycle. It is composed of the following two characteristic sections.

1) Those portions which marked red have a longer spatial expansion. Such a condition prevails when the spatial distance $|\boldsymbol{u}_k - \boldsymbol{u}_i|$ between the switching state vector and the induced voltage is short. This results in a slow displacement of the current vector, and it takes time to reach the next boundary. The average switching frequency is then low.
2) Different conditions exist at portions marked blue: large spatial distances between the switching state vector and

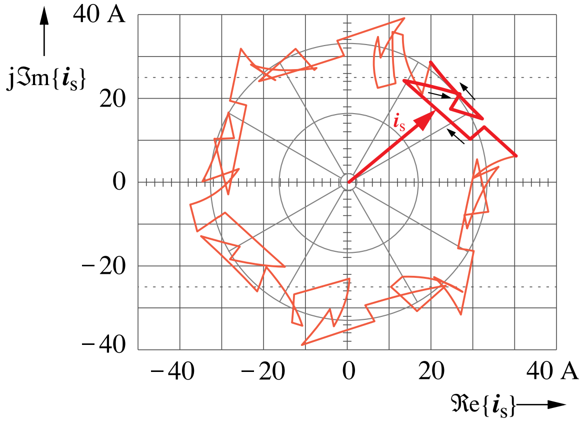

Fig. 14. Stator current trajectory at space vector modulation.

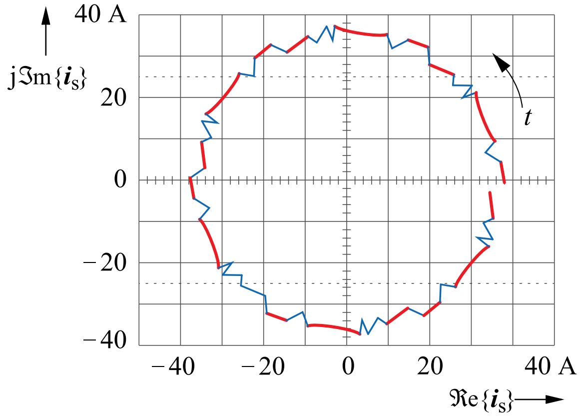

Fig. 15. Stator current trajectory at predictive control.

the induced voltage create a fast displacement of the current vector. The next boundary transition occurs within short time.

It is particularly the extended portions of the current trajectory with $|\boldsymbol{u}_k - \boldsymbol{u}_i|$ being small that let the average switching frequency reduce. The comparison in Fig. 16 of predictive control and synchronous optimal modulation shows that both methods achieve low harmonic distortion at low switching frequency. The maximum switching frequency is 215 Hz.

A normalized value d of the current distortion is displayed in Fig. 16. The definition takes into account that the rms harmonic current within a fundamental period T

$$I_{\mathbf{hrms}} = \sqrt{{}^{1}\!/_{T} \int_{(T)} \left[i\left(t\right) - i_1\left(t\right)\right]^2 dt} \qquad (25)$$

does not only depend on the performance of the pulse width modulator but also depend on the impedance of the machine. This influence is eliminated when the distortion factor

$$d = I_{\mathbf{h\ rms}} / I_{\mathbf{h\ rms\ six-step}} \qquad (26)$$

is used as a figure of merit. It refers the distortion current (25) of a given switching sequence to the distortion current i_h six-step of the same machine operated in the six-step mode as shown in Fig. 8.

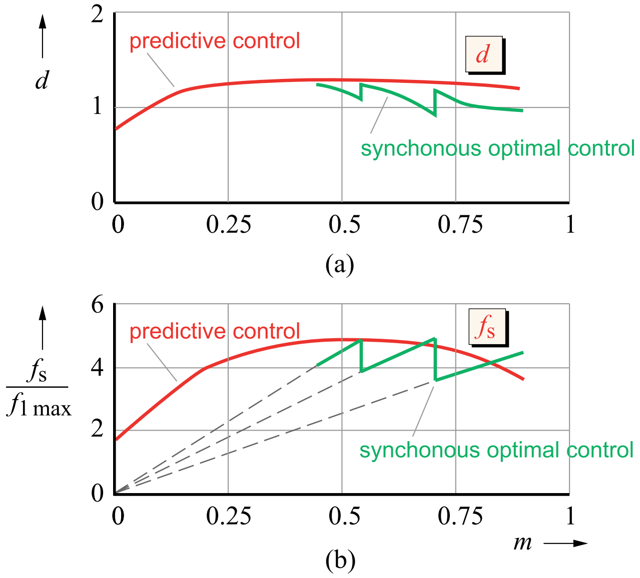

Fig. 16. Performance of optimal modulation methods. (a) Distortion factor d. (b) Normalized switching frequency f_s versus modulation index m. f_1 max = 50 Hz.

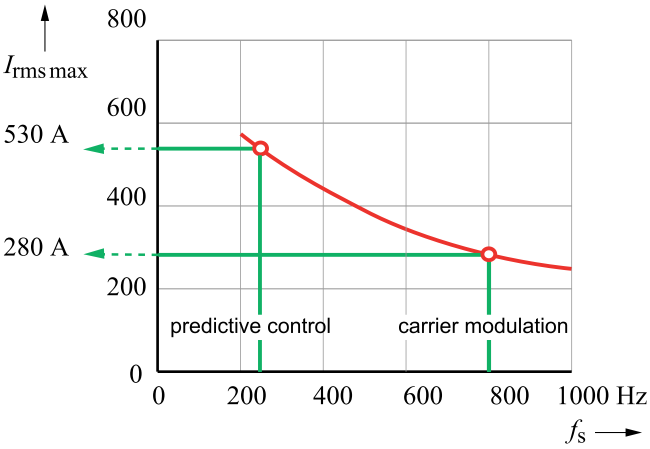

Fig. 17. Maximum achievable rms current versus switching frequency.

It is concluded that predictive control is an optimal modulation method.

VI. Experimental Results

Fig. 6 shows recorded waveforms at multistep prediction, and Fig. 9 shows the trajectories of the stator current vector within the rectangular boundary area at low speed, at the transition to the six-step mode, and in the six-step mode. Fig. 11 shows the smooth transition to predictive overmodulation. Fig. 17 shows that the maximum achievable rms current of a given drive system versus switching frequency is 1.9 times higher when the modulation changes from 800 Hz space vector modulation to 250 Hz predictive control. The trajectory of the current vector within the boundary is shown in Fig. 18. The structure is recorded in stationary coordinates, rotating with time. The direct transitions between the respective limits of the boundary area correspond to the trajectories in Fig. 15.

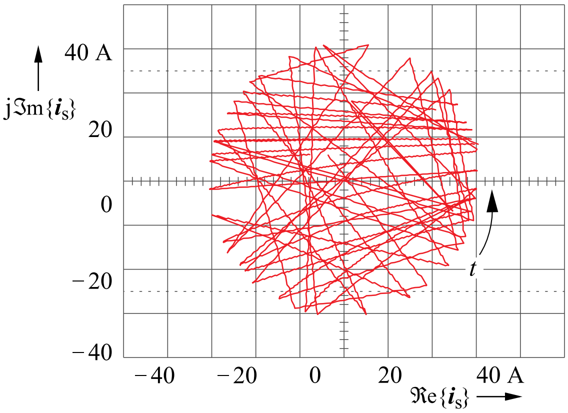

Fig. 18. Trajectory of the current vector within the boundary.

Fig. 13 compares the three-level waveforms at space vector modulation and synchronous optimal modulation, showing the stator current i_a, and of the inverter output voltage potential u_a at 200 Hz switching frequency.

Fig. 15 shows the stator current trajectory with the longer switching state durations highlighted in red, and Fig. 16 compares the performance of predictive control and synchronous optimal control.

VII. CONCLUSION

This article demonstrates that predictive control is an optimal modulation method. The method reduces both the switching frequency and the current distortion. Large dimensions of the respective boundaries provide persisting switching states whenever the reference vector and the current vector displace in a close spatial neighborhood at about the same angular velocity. The error magnitude then remains small for long durations such that boundary transitions get delayed. The average switching frequency reduces, but the harmonic distortion does not.

Applications in the upper power range are preferred candidates for predictive control. Switching frequencies of a few 100 Hz are required to minimize the switching losses. The dimensions of the respective boundaries are then high.

The switching frequency increases and the harmonic distortion reduces when operating at reduced boundary dimensions. One would tend to assume that harmonic distortions change in inverse proportion to the switching frequency. The opposite is true: small boundaries lead to more frequent boundary intersections, which lets the average switching frequency increase. Frequent interruptions of the long displacement intervals of the current vector impair the performance. Optimizing the switching sequence by displacing the switching instances becomes ineffective. Operating predictive control in the kHz range produces results similar to hysteresis control. These are worse than space vector modulation at the same switching frequency [21].

REFERENCES

[1] J. Holtz and S. Stadtfeld, “A predictive controller for the stator current vector of AC machines fed from a switched voltage source,” in *Proc. Int. Power Electron. Conf.*, 1983, pp. 1665–1675.

[2] J. Holtz and S. Stadtfeld, “An economic very high power PWM inverter for induction motor drives,” in *Proc. 1st Eur. Conf. Power Electron. Appl.*, 1985, pp. 3.75–3.80.

[3] M. R. Nasiri, S. Farhangi, and J. Rodríguez, “Model predictive control of a multilevel CHB STATCOM in wind farm application using diophantine equations,” *IEEE Trans. Ind. Electron.*, vol. 66, no. 2, pp. 1213–1223, Jun. 2019.

[4] X. Chen, W. Wu, N. Gao, H. S.-H. Chung, M. Liserre, and F. Blaabjerg, “Finite control set model predictive control for LCL-filtered grid-tied inverter with minimum sensors,” *IEEE Trans. Ind. Electron.*, vol. 67, no. 12, pp. 9980–9990, Dec. 2020.

[5] M. Aguirre, S. Kouro, C. A. Rojas, J. Rodriguez, and J. I. Leon, “Switching frequency regulation for FCS-MPC based on a period control approach,” *IEEE Trans. Ind. Electron.*, vol. 65, no. 7, pp. 5764–5773, Jun. 2018.

[6] T. Geyer, N. Oikonomou, G. Papafotiou, and F. Kieferndorf, “Model predictive pulse pattern control,” *IEEE Trans. Ind. Appl.*, vol. 48, no. 2, pp. 663–676, Mar./Apr. 2012.

[7] J. Holtz, “Advanced pulsewidth modulation and predictive control – An overview,” *IEEE Trans. Ind. Electron.*, vol. 63, no. 6, pp. 3837–3844, Jun. 2015.

[8] S. Richter, T. Geyer, and M. Morari, “Resource-efficient gradient methods for model predictive pulse pattern control on an FPGA,” *IEEE Trans. Control Syst. Technol.*, vol. 25, no. 3, pp. 828–841, May 2017.

[9] P. Karamanakos and T. Geyer, “Guidelines for the design of finite control set model predictive controllers,” *IEEE Trans. Power Electron.*, vol. 35, no. 7, pp. 7434–7450, Jul. 2020.

[10] *Proc. Symp. Predictive Control Power Electron. Elect. Drives PRECEDE*, vol. 63, no. 6, Oct. 2013.

[11] *Proc. Symp. Predictive Control Power Electron. Elect. Drives PRECEDE*, vol. 63, no. 7, Sep. 2017.

[12] *Proc. Symp. Predictive Control Power Electron. Elect. Drives PRECEDE*, vol. 63, no. 8, May 2019.

[13] M. Rivera, J. Rodriguez, and S. Vazquez, “16 papers in special section on predictive control in power converters and electrical drives—Part I,” *IEEE Trans. Ind. Electron.*, vol. 62, no. 6, pp. 3834–3984, Jun. 2016.

[14] M. Rivera, J. Rodriguez, and S. Vazquez, “17 papers in special section on predictive control in power converters and electrical drives—Part II,” *IEEE Trans. Ind. Electron.*, vol. 62, no. 7, pp. 4472–4640, Jul. 2016.

[15] M. Rivera, J. Rodriguez, and S. Vazquez, “18 papers in special section on predictive control in power converters and electrical drives—Part III,” *IEEE Trans. Ind. Electron.*, vol. 62, no. 8, pp. 5130–5312, Aug. 2016.

[16] R. Kennel and A. Linder, “Predictive control of inverter supplied electrical drives,” *Proc. 31st Annu. Power Electron. Spec. Conf.*, Jun. 2000, vol. 2, pp. 761–766.

[17] A. Linder, R. Kanchan, R. Kennel, and P. Stolze, *Model-Based Predictive Control of Electric Drives*. Göttingen, Germany: Cuvillier, 2010.

[18] T. Geyer, *Model Predictive Control of High Power Converters and Industrial Drives*. Hoboken, NJ, USA: Wiley, 2016.

[19] J. Holtz, W. Lotzkat, and A. Khambadkone, “On continuous control of PWM inverters in the overmodulation range with transition to the six-step mode,” *IEEE Trans. Power Electron.*, vol. 8, no. 4, pp. 546–553, Oct. 1993.

[20] J. Holtz and N. Oikonomou, “Closed-loop control of medium voltage drives operated with synchronous optimal pulse-width modulation,” *IEEE Trans. Ind. Appl.*, vol. 44, no. 1, pp. 115–123, Jan./Feb. 2008.

[21] B. K. Bose, Ed. *Power Electronics and Variable Frequency Drives*. Piscataway, NJ, USA: IEEE Press, 1997, pp. 138–208.